Article

Ordered and tunable Majorana-zero-mode lattice in naturally strained LiFeAs

Meng Li[1,2,7], Geng Li[1,2,3,4,7], Lu Cao[1,2,7], Xingtai Zhou[1,2], Xiancheng Wang[1,2], Changqing Jin[1,2,4], Ching-Kai Chiu[5], Stephen J. Pennycook[1,2], Ziqiang Wang[6✉] & Hong-Jun Gao[1,2,3,4✉]

Majorana zero modes (MZMs) obey non-Abelian statistics and are considered building blocks for constructing topological qubits[1,2]. Iron-based superconductors with topological bandstructures have emerged as promising hosting materials, because isolated candidate MZMs in the quantum limit have been observed inside the topological vortex cores[3–9]. However, these materials suffer from issues related to alloying induced disorder, uncontrolled vortex lattices[10–13] and a low yield of topological vortices[5–8]. Here we report the formation of an ordered and tunable MZM lattice in naturally strained stoichiometric LiFeAs by scanning tunnelling microscopy/spectroscopy. We observe biaxial charge density wave (CDW) stripes along the Fe–Fe and As–As directions in the strained regions. The vortices are pinned on the CDW stripes in the As–As direction and form an ordered lattice. We detect that more than 90 per cent of the vortices are topological and possess the characteristics of isolated MZMs at the vortex centre, forming an ordered MZM lattice with the density and the geometry tunable by an external magnetic field. Notably, with decreasing the spacing of neighbouring vortices, the MZMs start to couple with each other. Our findings provide a pathway towards tunable and ordered MZM lattices as a platform for future topological quantum computation.

The long quest for Majorana excitations[14–19] has been fuelled by recent experimental progress in material platforms where the localized MZM has been observed[16,20–23]. Among these platforms, iron-based superconductors are considered promising for the observation of clean and robust MZMs[3–5]. FeTe$_{0.55}$Se$_{0.45}$ was the first iron-based superconductor found to possess topological surface states[24,25]. The large Δ^2/E_F ratio, where Δ is the superconducting energy gap and E_F is the Fermi energy, enables the observation of an isolated MZM in the centre of a topological vortex[4], which exhibits nearly quantized plateaus in differential conductance[9]. Later on, stoichiometric iron pnictides were investigated and the existence of MZMs has been verified in CaKFe$_4$As$_4$ (ref. [8]) and LiFeAs (ref. [6]). Very recently, one-dimensional (1D) dispersing Majorana modes and MZMs have been observed in layered 2D superconductors with topological bandstructures[26–28]. However, these platforms suffer from alloying induced disorder, uncontrolled vortex lattice and a low yield of topological vortices, hindering their potential applications.

Biaxial CDW in naturally strained LiFeAs

We start with LiFeAs crystal, owing to its homogeneous bulk electronic structure, well defined cleaving surface and rich topological bandstructures[29]. LiFeAs belongs to the tetragonal crystal system, with lattice constants $a = b = 3.8$ Å and $c = 6.3$ Å (Fig. 1a). The As–As atomic direction defines the high-symmetry lattice orientations ([10] and [01] in Fig. 1b) of the mechanically cleaved nonpolar surface (Supplementary

Fig. 1). The existence of strain in the LiFeAs lattice leads to the formation of wrinkles[30] or electronic ordering such as CDWs[31]. We identified such strained regions with a biaxial CDW phase (Fig. 1c), which appears as a coexistence of small periodic (2.7 ± 0.2 nm) stripe patterns orienting along the Fe–Fe ([11]) direction (CDW$_{Fe–Fe}$) and large periodic (24.3 ± 0.9 nm) stripe patterns orienting along the As–As ([10]) direction (CDW$_{As–As}$). To corroborate the effect of the local strain on the formation of the CDWs, we performed atomically resolved scanning tunnelling microscopy (STM) imaging of the surface regions with and without the CDWs (Extended Data Fig. 1 and Supplementary Table 1). The distortion of the lattice in the CDW regions reveals the existence of biaxial and shear strain. The observed CDWs are reproducible in different LiFeAs samples and by using different STM instruments (Supplementary Fig. 2). Both CDW wavevectors can be clearly resolved in the Fourier transform image (Fig. 1d), with an angle of $45 \pm 1°$, breaking the C_4 rotation and reflection symmetry of the crystal lattice. Interestingly, the bright stripes of both CDW$_{Fe–Fe}$ and CDW$_{As–As}$ show abnormal splitting and recombination behaviour with increasing bias voltages near E_F (Extended Data Fig. 2), which are accompanied by a π phase shift in the stripe pattern (Extended Data Fig. 2c, d, k, p). The similar energy-dependent evolution of the stripes indicates that the two CDW phases are coupled with each other. We note that both CDW wavevectors are nondispersive with energy (Extended Data Fig. 2 and Supplementary Fig. 3), precluding other possibilities such as quasi-particle interference[32,33].

[1]Beijing National Center for Condensed Matter Physics and Institute of Physics, Chinese Academy of Sciences, Beijing, PR China. [2]School of Physical Sciences, University of Chinese Academy of Sciences, Beijing, PR China. [3]CAS Center for Excellence in Topological Quantum Computation, University of Chinese Academy of Sciences, Beijing, PR China. [4]Songshan Lake Materials Laboratory, Dongguan, PR China. [5]RIKEN Interdisciplinary Theoretical and Mathematical Sciences (iTHEMS), Wako, Japan. [6]Department of Physics, Boston College, Chestnut Hill, MA, USA. [7]These authors contributed equally: Meng Li, Geng Li, Lu Cao. ✉e-mail: wangzi@bc.edu; hjgao@iphy.ac.cn
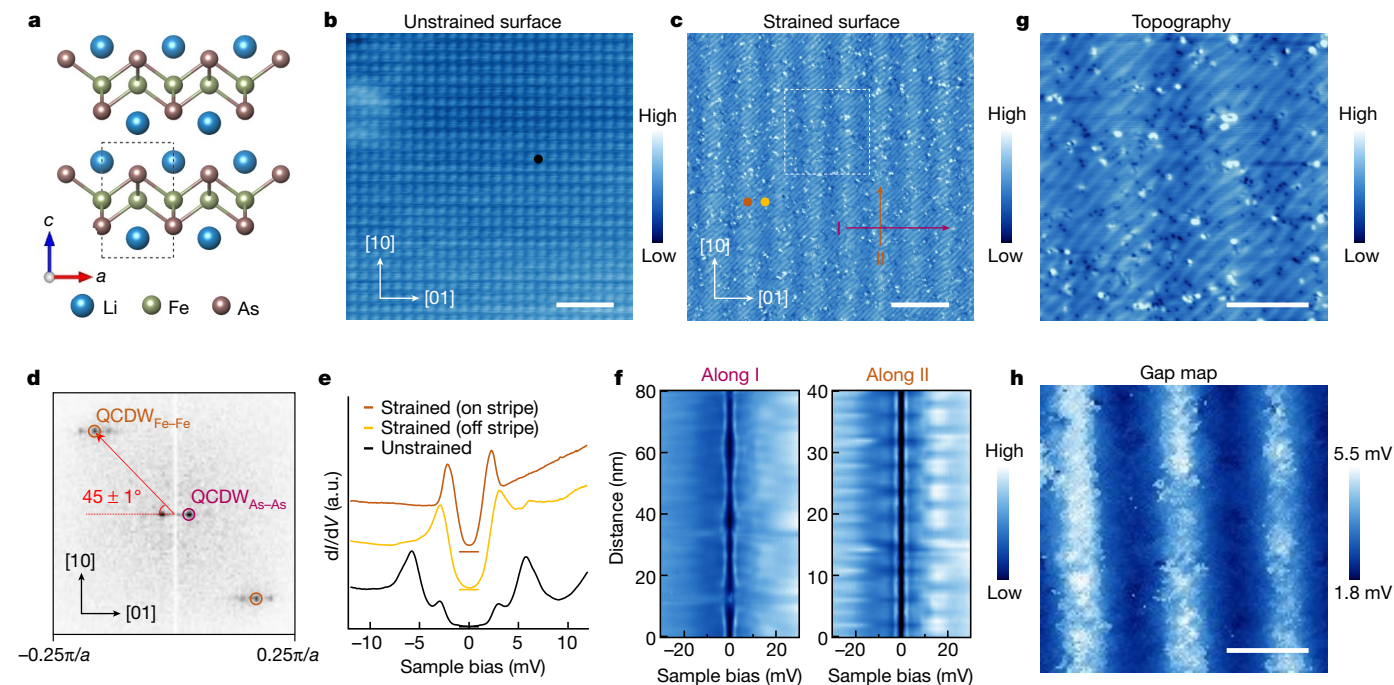
Fig. 1 | Crystalline structure, topographic image and superconducting behaviour of the unstrained and strained regions. a, Atomic model of the LiFeAs single crystal. **b**, **c**, STM images of unstrained (**b**) and strained (**c**) regions on a cleaved LiFeAs single crystal. Scanning settings for **b**: bias $V_s = -3$ mV and setpoint $I_t = 400$ pA; for **c**: $V_s = -30$ mV and $I_t = 50$ pA. **d**, Fourier transform image of **c**, showing the wavevectors of the CDW_{Fe-Fe} and CDW_{As-As}, labelled as $QCDW_{Fe-Fe}$ and $QCDW_{As-As}$. The angle between the wavevectors of CDW_{Fe-Fe} and CDW_{As-As} is $45 \pm 1°$. **e**, Typical dI/dV spectra taken at the bright stripe (brown curve), off the bright stripe (yellow curve) of the CDW_{As-As} and in the unstrained region (black curve). The dI/dV spectra are vertically offset for clarity, and the horizontal solid lines represent positions of zero density of states for each of the curves. The bright stripe region has smaller superconducting gap size and higher in-gap density of states than that of the off-stripe region. **f**, Intensity maps of the dI/dV spectra along arrows I (left) and II (right) in **c**. The superconducting gap value is modulated by the large stripes of the CDW_{As-As}, whereas the CDW_{Fe-Fe} pattern modulates only the height of superconducting coherence peaks. **g**, Magnified STM image of the white dashed box in **c** ($V_s = -30$ mV, $I_t = 50$ pA). **h**, Superconducting gap map of the same region in **g**, showing reduced superconducting gap sizes on the bright As–As stripes. Scale bars: 2 nm (**b**), 40 nm (**c**), 20 nm (**g**, **h**). a.u., arbitrary units.

To investigate the influence of the biaxial CDW phase on the superconducting behaviour, we measure the dI/dV spectra in different regions. In the unstrained region (black dot in Fig. 1b), the dI/dV spectrum shows the multigap feature of LiFeAs, with a large gap of approximately 5.8 meV and a small gap of around 2.9 meV (black curve in Fig. 1e), consistent with previous reports[10,32]. In the strained region, the superconducting gap on the bright stripe (2.1 ± 0.1 mV) of CDW_{As-As} is smaller than that off the stripe (3.4 ± 0.2 mV) (brown and yellow curves in Fig. 1e). Importantly, the two CDW orders affect the local superconductivity in very different ways. Whereas the CDW_{As-As} clearly modulates the superconducting gap size (Fig. 1f, left), the CDW_{Fe-Fe} only modulates the intensity of the superconducting coherence peak without altering the gap size (Fig. 1f, right). The modulation of the superconducting gap suggests a strong coupling of the CDW to the superconductivity. We note that the periodicity of CDW_{As-As} is much larger than the superconducting coherence length (4.8 nm)[34] in LiFeAs, and the modulation of superconducting behaviour at such large scale is rare. To provide a straightforward visualization of the coupling between the CDW and the superconductivity, we conduct a series of dI/dV maps at different energies and extract the superconducting gap values across the region in Fig. 1g. The superconducting gap map (Fig. 1h) shows clearly the modulation of the superconducting gap size by CDW_{As-As}.

Formation of MZM lattice

We then apply an external field of 0.5 T normal to the sample surface, and find magnetic vortices emerging exclusively on the bright stripes of CDW_{As-As} (Fig. 2a). The strong pinning effect of the vortices by the CDW_{As-As} stripes is probably due to the suppressed superconducting gap in the bright As–As stripe regions. We take dI/dV spectra across a typical vortex (along the red arrow in Fig. 2a), and find sharp zero-bias conductance peaks (ZBCPs) near the vortex centre in the waterfall plot (Fig. 2b) and intensity map (Fig. 2c), together with an 'X'-like feature and discrete peaks on the two sides of the ZBCP. The ZBCP decays without splitting when the tip moves away from the vortex centre (Fig. 2c), which is reminiscent of a MZM in the vortex core of other iron-based superconductors with topological surface states[4,6,8]. To better differentiate the energy positions of the discrete peaks, we show the negative second derivative of the waterfall plot (Fig. 2d) and the intensity map (Fig. 2e) of the dI/dV curves in Fig. 2b, c. A series of discrete vortex core states can be resolved (Fig. 2d, e), suggesting that the vortex is in the quantum limit[4,35]. The spatial evolution of the peak energy of the core states roughly follow straight lines (dashed vertical lines in Fig. 2e), as expected for the low-lying Caroli–de Gennes–Matricon (CdGM) bound states[36–38]. The other vortices exhibit similar spectroscopic features (Supplementary Fig. 4).

To determine the energies of the vortex core states, five individual dI/dV spectra close to the centre of the vortex core (red arrows in Fig. 2d) are replotted in Fig. 2f. The discrete vortex core states manifest as peaks marked by the vertical arrows. The CdGM states are bound states inside the superconducting gap and spatially localized in a vortex core. In an ordinary vortex, the energy of the bound states is half-integer quantized, $E_j = jE_0$, where $j = \pm1/2, \pm3/2, \ldots$ is the total angular momentum quantum number. However, for a topological vortex, the topological Dirac fermion surface states contribute an additional π phase, leading to a half-integer shift in the quantum number of the total angular momentum. As a result, the energy of the CdGM states is integer-quantized, $E_j = jE_0$, where $j = 0, \pm1, \pm2, \ldots$ in the
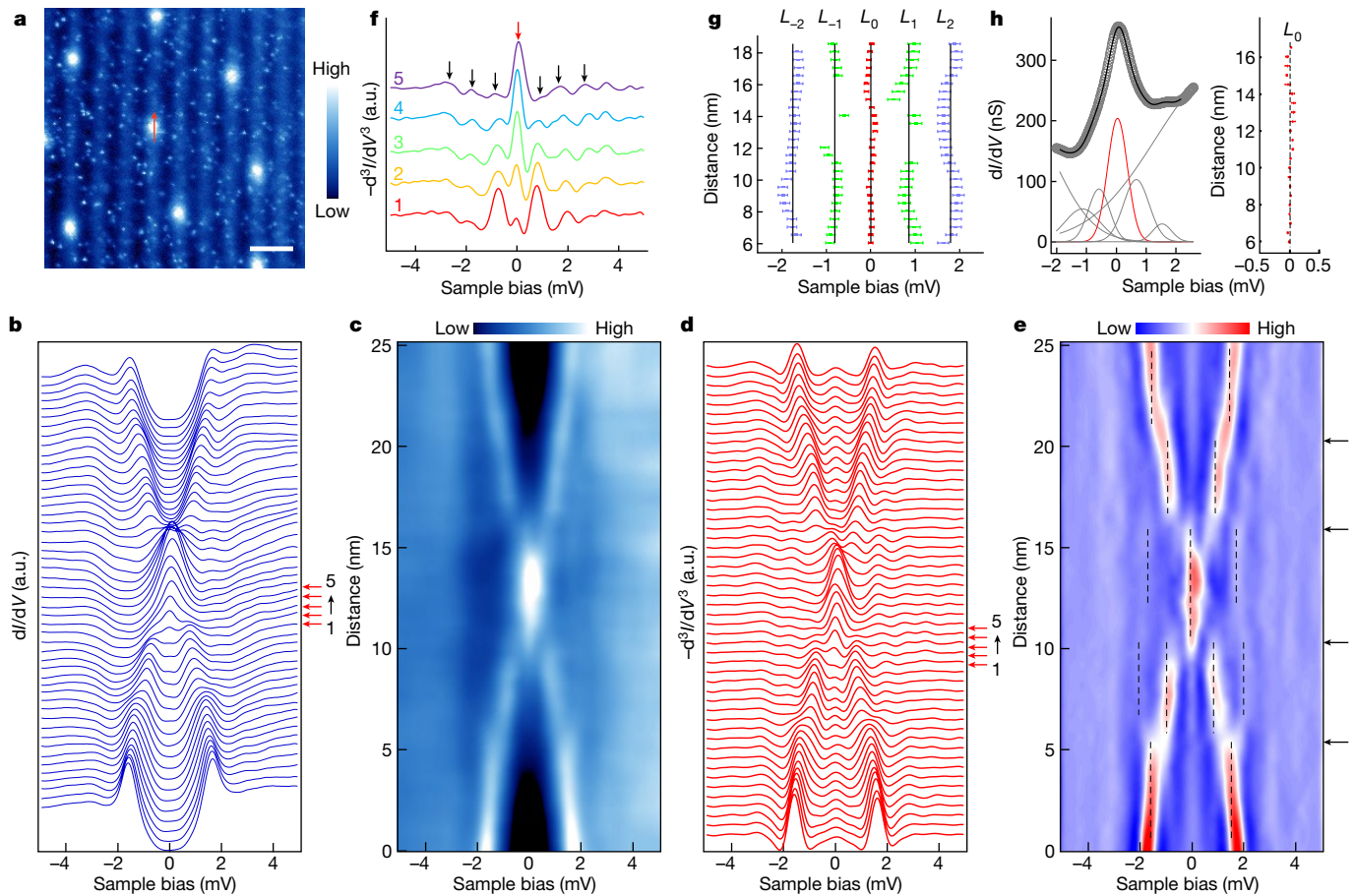
Fig. 2 | dI/dV map of the vortices and the analysis of the vortex bound states under 0.5 T. a, dI/dV map of the biaxial CDW region ($V_s = 0$ mV), showing that the vortices are pinned to the bright As–As stripes. Scale bar, 40 nm. **b**, **c**, Waterfall plot (**b**) and intensity map (**c**) of the dI/dV spectra along the red arrow in **a**, showing sharp ZBCPs at the centre of the vortex. **d**, **e**, Negative second derivative of **b** (**d**) and **c** (**e**), indicating that a series of discrete peaks are located on the two sides of the ZBCP. The dashed vertical lines in **e** outline the positions of the discrete peaks. Following the dashed vertical lines, the spatial evolvement of the discrete peaks is divided into sections, as marked by the horizontal black arrows. The peak positions show slight spatial dispersion from straight lines. **f**, Negative second derivative of the five typical dI/dV spectra (red arrows in **d**) taken close to the centre of the vortex in **a**. The ZBCP is highlighted by a vertical red arrow, and the other discrete energy bound states are highlighted by vertical black arrows. **g**, Statistical analysis of the peak positions in **e**. Five energy bound states at -1.76 ± 0.11 (L_{-2}), -0.81 ± 0.09 (L_{-1}), 0.00 ± 0.06 (L_0), 0.86 ± 0.10 (L_1), and 1.80 ± 0.13 (L_2) meV are extracted. **h**, Left, the black circles show a typical dI/dV spectrum near the vortex core, with the extracted L_0 state from **d** deviating from zero energy. The red peak is the calibrated ZBCP by multi-Gaussian peak fitting. The grey lines indicate the fitted CdGM states and the background. The black solid line is the fitted curve. Right, spatial distribution of the calibrated L_0 state, showing robust ZBCPs.

topological vortex. The average values and the deviations of the core states are summarized in Fig. 2g. Five discrete states at -1.76 ± 0.11 (L_{-2}), -0.81 ± 0.09 (L_{-1}), 0.00 ± 0.06 (L_0), 0.86 ± 0.10 (L_1), and 1.80 ± 0.13 (L_2) meV are extracted, which approximately follow an integer-quantized sequence. Different from conventional CdGM states, the vortex core states exhibit weak spatial dispersions (horizontal black arrows in Fig. 2e and the extracted core states in Fig. 2g). To accurately determine the energy of the L_0 state, we decompose the original dI/dV spectra into multiple Gaussian-like peaks[7,38] (Supplementary Fig. 5 and Fig. 2h, left). Utilizing this approach, we calibrate the L_0 states (Fig. 2h, right), and find that they locate at the Fermi energy. The robust ZBCP with a decaying intensity away from the vortex centre is strong evidence of a MZM in a topological vortex[4]. The full-width at half-maximum (FWHM) of the fitted ZBCPs is approximately 0.4 meV, which is comparable to the energy resolution of our instrument (0.3 meV). These results strongly support the existence of MZMs in the vortex centres.

We then investigate the influence of the CDW stripes on the dI/dV spectra of the vortices for further understanding of the spatial evolution of the CdGM states. In the negative second derivative of the intensity maps of dI/dV spectra across a topological vortex (Extended Data

Fig. 3a), the dispersion happens at positions marked by the horizontal white dashed lines (Extended Data Fig. 3a, left). Remarkably, these horizontal lines are in good agreement with the positions of the dark Fe–Fe stripes (see height profile in Extended Data Fig. 3a, right), indicating that the $CDW_{Fe–Fe}$ has strong influence on the vortex core states. The CdGM states are usually understood as eigenstates of a vortex under rotation symmetry. Once the rotation and reflection symmetries are broken, hybridization between the eigenstates can cause the spatial dispersions of the CdGM states (Fig. 2g and Extended Data Fig. 3b). This is, to our knowledge, the first experimental observation of hybridization between vortex core states. The MZMs, however, do not disperse and remain at zero energy, consistent with its topologically protected robustness against local perturbations.

Increasing the external field to 3 T, more vortices emerge, pinned to the bright $CDW_{As–As}$ stripes (Supplementary Fig. 6). Figure 3a shows the intensity map of dI/dV spectra across a topological vortex in the upper panel and an ordinary vortex in the lower panel. Remarkably, its negative second derivative shows a half-integer-level shift in the energy of the vortex core states (Fig. 3b), which was considered as strong evidence distinguishing the topological vortex and
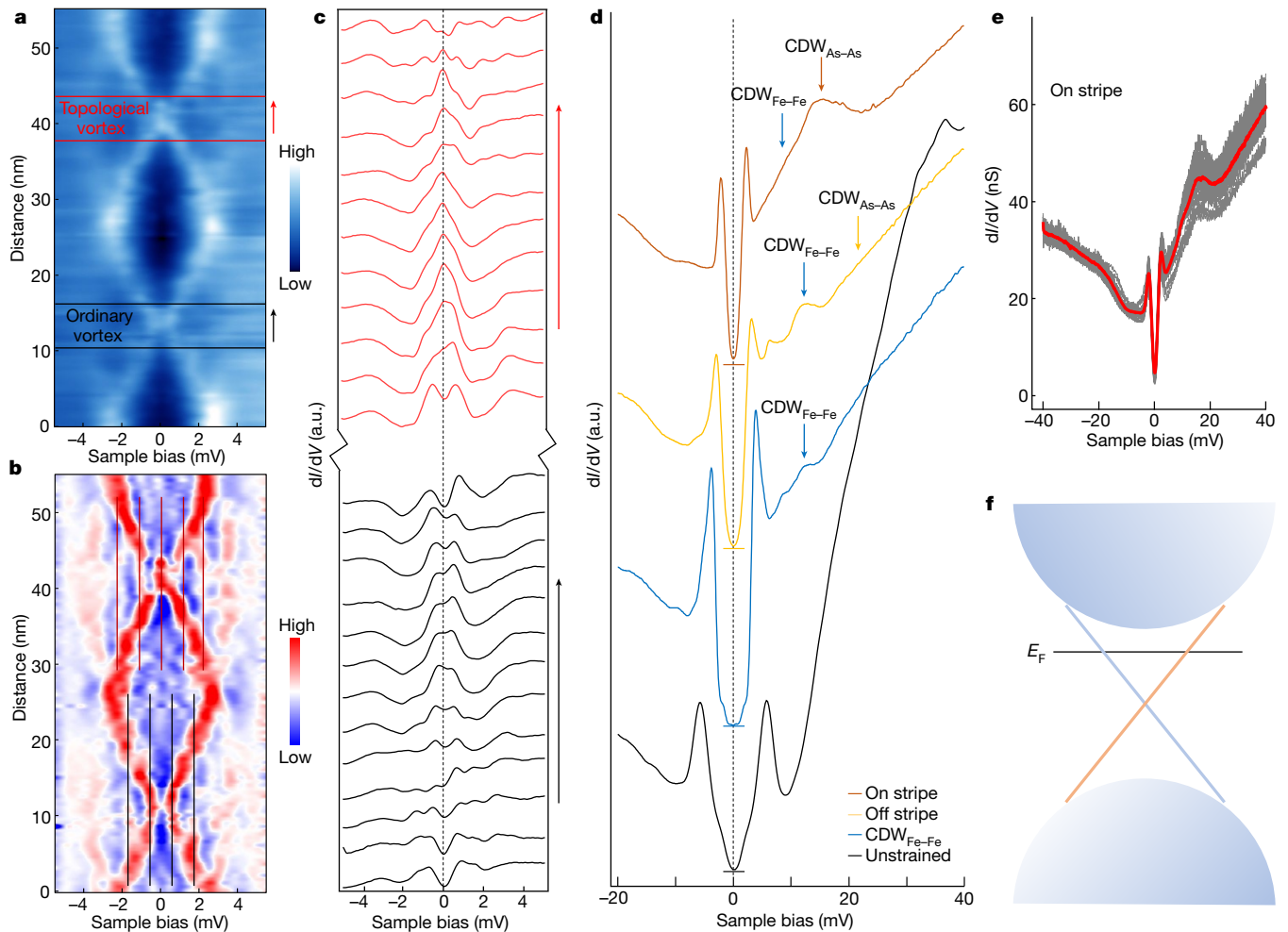
Fig. 3 | Analysis of the dI/dV spectra along a linecut across two neighbouring vortices and the origin of the MZMs. a, Intensity plot of dI/dV spectra across two neighbouring vortices along a CDW$_{As-As}$ stripe under 3 T. **b**, Negative second derivative of **a**. The vertical dashed lines highlight the vortex core states. The upper vortex is topological with a ZBCP, and the lower vortex is ordinary. The discrete peaks of the ordinary vortex show half-integer level shift with that of the topological vortex. **c**, Magnification of the individual dI/dV spectrum taken at regions close to the two vortex cores, as marked by the horizontal red and black dashed lines in **a**. The vertical black dashed line labels the zero bias. **d**, Wide-range dI/dV spectra at the on As–As stripe (brown) and off As–As stripe (yellow) locations in a biaxial CDW region, the uniaxial CDW$_{Fe-Fe}$ region (blue), and the unstrained region (black), respectively. The horizontal

solid lines highlight the positions of zero density of states for each curve. The big hump at approximately 33 mV of the black curve assigned to the band top of d_{xy} in the unstrained region is absent in the uniaxial CDW$_{Fe-Fe}$ and biaxial CDW regions, suggesting large band renormalization effects that also reduce the slope of the density states increase with energy. The coherence peaks of CDW$_{As-As}$ and CDW$_{Fe-Fe}$ are highlighted by vertical arrows. **e**, Averaged dI/dV spectra taken on the bright As–As stripes in the biaxial CDW region. The linear dispersion of the topological surface states can be related to an approximately V-shaped spectral shape with the Dirac point located at approximately −10 meV. **f**, Schematic of the bandstructure of the strained LiFeAs around the Γ point. The bulk states are gapped out by the biaxial CDW order, giving rise to the topological insulator surface states.

the ordinary vortex[38]. We also plot the individual dI/dV spectra at the two vortex cores as marked by the red and black dashed lines in Fig. 3a. A sharp ZBCP is seen in the topological vortex (Fig. 3c, top). However, the ZBCP is absent for the ordinary vortex (Fig. 3c, bottom). We measure the dI/dV spectra at the centre of each topological vortex, as shown in Extended Data Fig. 4. All spectra show similar profiles, suggesting the electronic structure of the vortices are uniform. More than 90% of vortices are topological vortices, giving rise to an ordered MZM lattice (Extended Data Fig. 4). This conclusion holds for different magnetic fields from 0.5 to 6 T (see Methods and Extended Data Figs. 5, 6).

Origin of the MZMs in pinned vortices

Now we discuss the possible origin of the MZM lattice. The topological nature of the pristine LiFeAs is very intriguing and contains two parts. First there is a set of helical Dirac fermion topological surface

states akin to those in a 3D topological insulator, which are located closest to the Fermi level. Second and unique to LiFeAs, there is a set of bulk Dirac fermion states sitting approximately 10 meV above the Fermi level, which is characteristic of a topological Dirac semimetal. This dual topological nature complicates the vortex core spectrum for the unstrained LiFeAs, which appeared gapless, and prohibited the identification of the discrete vortex core states[6,10,39]. To uncover the electronic structure of the strained LiFeAs, we take wide energy scale dI/dV spectra in the unstrained (lower region in Extended Data Fig. 7) and the CDW$_{Fe-Fe}$ (upper-left region in Extended Data Fig. 7) regions, and in the biaxial CDW region on and off the As–As stripes (Fig. 3d and Extended Data Fig. 8). In the unstrained region, a hump can be recognized at an energy of approximately 33 meV (black curves in Fig. 3d and Supplementary Fig. 7), which is assigned to the top of d_{xy} band[6]. In the strained regions, however, the hump feature disappears (brown, yellow and blue curves in Fig. 3d and Supplementary Fig. 7), indicating a renormalization in the local electronic structure by the CDW orders.
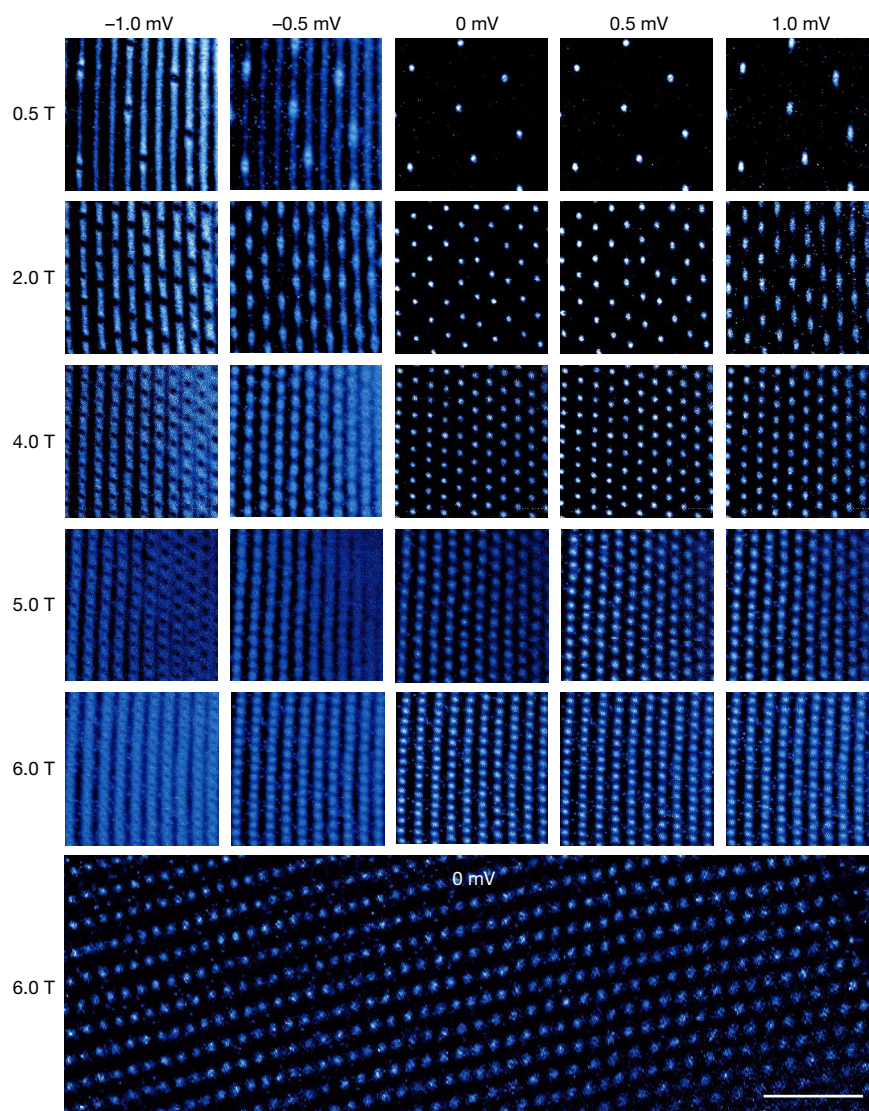
Fig. 4 | Tuning the MZM lattice with external magnetic fields. Series of d*I*/d*V* maps of the MZM vortices in the biaxial CDW region under magnetic fields of 0.5 T, 2 T, 4 T, 5 T and 6 T and at bias voltages from −1.0 mV to 1.0 mV. Large-scale, ordered MZM lattice of different spacing and density is formed when increasing external magnetic fields. The scanning areas are 0.24 μm × 0.24 μm. Bottom, micrometre-sized ordered MZM lattice under 6 T. The scanning area is 0.26 μm × 0.82 μm. Scale bar, 0.1 μm.

In the uniaxial $CDW_{Fe–Fe}$ region, the coherence peak of the $CDW_{Fe–Fe}$ is identified at approximately 10 mV (blue arrow in Fig. 3d), in accordance with previous reports[31]. In the biaxial CDW region, additional peaks indicated by the brown and yellow arrows can be resolved (Fig. 3d and Supplementary Fig. 7). This new peak corresponds to the coherence peak of the $CDW_{As–As}$ order, because it is strongly modulated by the As–As stripes (Extended Data Fig. 8).

The above-assigned CDW coherence peaks, together with the superconducting coherence peaks, lie on a background of a 'V'-shaped envelope in the d*I*/d*V* spectra (Fig. 3e and Supplementary Fig. 8) with the dip locating at approximately −10 mV. This V-shaped envelope is a signature for the existence of a Dirac cone[4] in two dimensions. These observations together suggest that the remarkable changes in the electronic structure in the strained biaxial CDW regions come from the breaking of the rotation and reflection symmetries, which gaps out the bulk Dirac cone protected by the rotation symmetry. This turns the local electronic structure of the stoichiometric, but strained, biaxial CDW regions into a strong topological insulator exclusively, hosting the prominent helical Dirac fermion topological surface states (Fig. 3f)

and generates the robust topological Majorana vortices in the superconducting state. This conclusion is corroborated by the fact that in the unstrained and the uniaxial $CDW_{Fe–Fe}$ regions, only ordinary vortices with no MZMs are observed (Extended Data Fig. 9).

Tuning the MZM lattice with magnetic fields

Finally, we demonstrate the tunability of the ordered MZM lattice by external magnetic field. The ordered MZM lattice originates from the fact that all vortices are firmly pinned to the periodic bright stripes along the As–As direction (Fig. 4). At 0.5 T, the vortices have low density and arrange themselves amorphously. Upon increasing the magnetic field to 5 T, the MZM lattice gradually evolves into the triangular lattice shape. It should be noted that at −0.5 mV, the vortices are ring-shaped, whereas at 0 and 0.5 mV they appear as solid circles. The d*I*/d*V* maps reflect the wavefunctions of the bound states inside the vortex cores, which are described by Bessel functions[36,40,41]. The ring structure for the negative energy branch suggests that the chemical potential lies above the Dirac point[8,41] (Fig. 3f). The pinning effect of

Article

the vortices by the stripes is so strong that the mobility of the vortices is limited to only one direction–along the stripe. By increasing the field, the newly emerged vortices are 'doped' into the bright stripes, forming regular 1D vortex chains. The inter-chain vortex interactions are fixed owing to the pinning effect, whereas the intra-chain vortex interactions can be manipulated by the applied magnetic field (Supplementary Fig. 9). The strong pinning effect provides better control over the vortex motion, as compared to the traditional 2D disordered Abrikosov vortex lattices[10,11]. It is further demonstrated that the ordered lattice is tunable by the external magnetic fields. The overall size of the MZM lattice can be brought up to the micrometre level, only limited by the STM scanning capability, and could extend to an even larger area (Fig. 4, bottom). We have also obtained the correlation between the vortex spacing and the dI/dV spectra of the vortices, indicating a coupling between the MZMs under high magnetic fields (Extended Data Fig. 10).

In summary, we have observed a micrometre-scale MZM lattice on naturally strained LiFeAs surface. The vortices are pinned to the $CDW_{As–As}$ stripes, giving rise to an ordered Abrikosov vortex lattice. We have demonstrated that the ordered lattice is tunable by external magnetic fields and observed the coupling between the MZMs under high magnetic fields. Our findings provide a promising platform for manipulating and braiding MZMs in the future. The large ordered array of MZMs can be suitable for realizing the 'braiding by measurement only' algorithm using interferometry[42].

Online content

1. Kitaev, A. Y. U. Fault-tolerant quantum computation by anyons. *Ann. Phys.* **303**, 2–30 (2003).
2. Nayak, C. et al. Non-Abelian anyons and topological quantum computation. *Rev. Mod. Phys.* **80**, 1083–1159 (2008).
3. Zhang, P. et al. Observation of topological superconductivity on the surface of an iron-based superconductor. *Science* **360**, 182–186 (2018).
4. Wang, D. F. et al. Evidence for Majorana bound states in an iron-based superconductor. *Science* **362**, 333–335 (2018).
5. Machida, T. et al. Zero-energy vortex bound state in the superconducting topological surface state of Fe(Se,Te). *Nat. Mater.* **18**, 811–815 (2019).
6. Kong, L. Y. et al. Majorana zero modes in impurity-assisted vortex of LiFeAs superconductor. *Nat. Commun.* **12**, 4146 (2021).
7. Liu, Q. et al. Robust and clean Majorana zero mode in the vortex core of high-temperature superconductor $(Li_{0.84}Fe_{0.16})OHFeSe$. *Phys. Rev. X* **8**, 041056 (2018).
8. Liu, W. Y. et al. A new Majorana platform in an Fe–As bilayer superconductor. *Nat. Commun.* **11**, 5688 (2020).
9. Zhu, S. Y. et al. Nearly quantized conductance plateau of vortex zero mode in an iron-based superconductor. *Science* **367**, 189–192 (2020).
10. Hanaguri, T. et al. Scanning tunneling microscopy/spectroscopy of vortices in LiFeAs. *Phys. Rev. B* **85**, 214505 (2012).
11. Fente, A. et al. Influence of multiband sign-changing superconductivity on vortex cores and vortex pinning in stoichiometric high-T_c $CaKFe_4As_4$. *Phys. Rev. B* **97**, 134501 (2018).
12. Chiu, C. K. et al. Scalable Majorana vortex modes in iron-based superconductors. *Sci. Adv.* **6**, eaay0443 (2020).
13. Zhang, S. T. S. et al. Vector field controlled vortex lattice symmetry in LiFeAs using scanning tunneling microscopy. *Phys. Rev. B* **99**, 161103 (2019).
14. Kitaev, A. Y. U. Unpaired Majorana fermions in quantum wires. *Phys. Uspekhi* **44**, 131–136 (2001).
15. Read, N. & Green, D. Paired states of fermions in two dimensions with breaking of parity and time-reversal symmetries and the fractional quantum Hall effect. *Phys. Rev. B* **61**, 10267–10297 (2000).
16. Fu, L. & Kane, C. L. Superconducting proximity effect and Majorana fermions at the surface of a topological insulator. *Phys. Rev. Lett.* **100**, 096407 (2008).
17. Lutchyn, R. M., Sau, J. D. & Das Sarma, S. Majorana fermions and a topological phase transition in semiconductor–superconductor heterostructures. *Phys. Rev. Lett.* **105**, 077001 (2010).
18. Oreg, Y., Refael, G. & von Oppen, F. Helical liquids and Majorana bound states in quantum wires. *Phys. Rev. Lett.* **105**, 177002 (2010).
19. Potter, A. C. & Lee, P. A. Multichannel generalization of Kitaev's Majorana end states and a practical route to realize them in thin films. *Phys. Rev. Lett.* **105**, 227003 (2010).
20. Mourik, V. et al. Signatures of Majorana fermions in hybrid superconductor–semiconductor nanowire devices. *Science* **336**, 1003–1007 (2012).
21. Nadj-Perge, S. et al. Observation of Majorana fermions in ferromagnetic atomic chains on a superconductor. *Science* **346**, 602–607 (2014).
22. Xu, J. P. et al. Experimental detection of a Majorana mode in the core of a magnetic vortex inside a topological insulator–superconductor $Bi_2Te_3/NbSe_2$ heterostructure. *Phys. Rev. Lett.* **114**, 017001 (2015).
23. Deng, M. T. et al. Majorana bound state in a coupled quantum-dot hybrid-nanowire system. *Science* **354**, 1557–1562 (2016).
24. Wang, Z. J. et al. Topological nature of the $FeSe_{0.5}Te_{0.5}$ superconductor. *Phys. Rev. B* **92**, 115119 (2015).
25. Wu, X. X. et al. Topological characters in $Fe(Te_{1−x}Se_x)$ thin films. *Phys. Rev. B* **93**, 115129 (2016).
26. Yuan, Y. H. et al. Evidence of anisotropic Majorana bound states in $2M-WS_2$. *Nat. Phys.* **15**, 1046–1051 (2019).
27. Kezilebieke, S. et al. Topological superconductivity in a van der Waals heterostructure. *Nature* **588**, 424–428 (2020).
28. Nayak, A. K. et al. Evidence of topological boundary modes with topological nodal-point superconductivity. *Nat. Phys.* **17**, 1413–1419 (2021).
29. Zhang, P. et al. Multiple topological states in iron-based superconductors. *Nat. Phys.* **15**, 41–47 (2019).
30. Cao, L. et al. Two distinct superconducting states controlled by orientation of local wrinkles in LiFeAs. *Nat. Commun.* **12**, 6312 (2021).
31. Yim, C. M. et al. Discovery of a strain-stabilised smectic electronic order in LiFeAs. *Nat. Commun.* **9**, 2602 (2018).
32. Allan, M. P. et al. Anisotropic energy gaps of iron-based superconductivity from intraband quasiparticle interference in LiFeAs. *Science* **336**, 563–567 (2012).
33. Allan, M. P. et al. Identifying the 'fingerprint' of antiferromagnetic spin fluctuations in iron pnictide superconductors. *Nat. Phys.* **11**, 177–182 (2015).
34. Zhang, J. L. et al. Upper critical field and its anisotropy in LiFeAs. *Phys. Rev. B* **83**, 174506 (2011).
35. Hayashi, N., Isoshima, T., Ichioka, M. & Machida, K. Low-lying quasiparticle excitations around a vortex core in quantum limit. *Phys. Rev. Lett.* **80**, 2921–2924 (1998).
36. Caroli, C., Degennes, P. G. & Matricon, J. Bound fermion states on a vortex line in a type-II superconductor. *Phys. Lett.* **9**, 307–309 (1964).
37. Fan, P. et al. Observation of magnetic adatom-induced Majorana vortex and its hybridization with field-induced Majorana vortex in an iron-based superconductor. *Nat. Commun.* **12**, 1348 (2021).
38. Kong, L. Y. et al. Half-integer level shift of vortex bound states in an iron-based superconductor. *Nat. Phys.* **15**, 1181–1187 (2019).
39. Hu, L. H., Wu, X. X., Liu, C. X. & Zhang, R. X. Competing vortex topologies in iron-based superconductors. Preprint at https://arxiv.org/abs/2110.11357 (2021).
40. Cheng, M., Lutchyn, R. M., Galitski, V. & Das Sarma, S. Tunneling of anyonic Majorana excitations in topological superconductors. *Phys. Rev. B* **82**, 094504 (2010).
41. Kawakami, T. & Hu, X. Evolution of density of states and a spin-resolved checkerboard-type pattern associated with the Majorana bound state. *Phys. Rev. Lett.* **115**, 177001 (2015).
42. Bonderson, P., Freedman, M. & Nayak, C. Measurement-only topological quantum computation via anyonic interferometry. *Ann. Phys.* **324**, 787–826 (2009).

Methods

Single-crystal growth

High-quality LiFeAs single crystals were synthesized by using the self-flux method. A LiFeAs crystal was mounted on an STM sample holder in a glove box and transferred to an ultrahigh-vacuum chamber. The crystal was cleaved in situ. The low cleaving temperature of 10 K is for a higher chance to find the strained regions hosting the CDWs compared with the room-temperature cleavage. After cleavage, the sample was immediately transferred to the STM scanner.

STM/S experiments

The STM/S measurements were conducted in an ultralow-temperature STM system equipped with 9-2-2 T vectorial magnets. Tungsten tips were etched chemically and calibrated on Au(111) surfaces before use. The dI/dV spectra and maps were obtained by a standard lock-in technique with a modulation voltage of 0.1 mV at 973.0 Hz. All the images, spectra and dI/dV maps were taken at 400 mK.

Fitting method

Linear least-squares fitting was used to determine the positions of the vortex core states. Five Gaussian peaks representing the in-gap bound states were used for the fitting of each spectrum. In the fitting process, all the parameters of the Gaussian peaks are set free. The peak positions of the bound states were extracted from the fitting results.

Statistics of the topological vortices

The determination of percentage of topological vortices in the biaxial CDW region was performed by the measurement of dI/dV spectra of 51 vortices under 3 T. A smaller region that contains three to four vortices within the area were mapped at zero energy so that the centres of the vortex cores could be accurately located. The spectra were all taken under the same scanning settings. The spectra were further calibrated by the multi-Gaussian peak fitting method to accurately locate the positions of the bound states. The same strategy was used for different fields from 0.5 to 6 T, and the topological vortices were always higher than 90% of the total number.

Author contributions H.-J.G. designed the experiments and supervised the project. X.W. and C.J. prepared samples. M.L., G.L., L.C. and X.Z. performed STM experiments with the guidance of H.-J.G. G.L., C.-K.C., S.J.P., Z.W. and H.-J.G. did data analysis and wrote the manuscript. All of the authors participated in analysing experimental data, plotting figures and writing the manuscript.

a Unstrained
2 nm

b Uniaxial CDW$_{Fe-Fe}$
4 nm

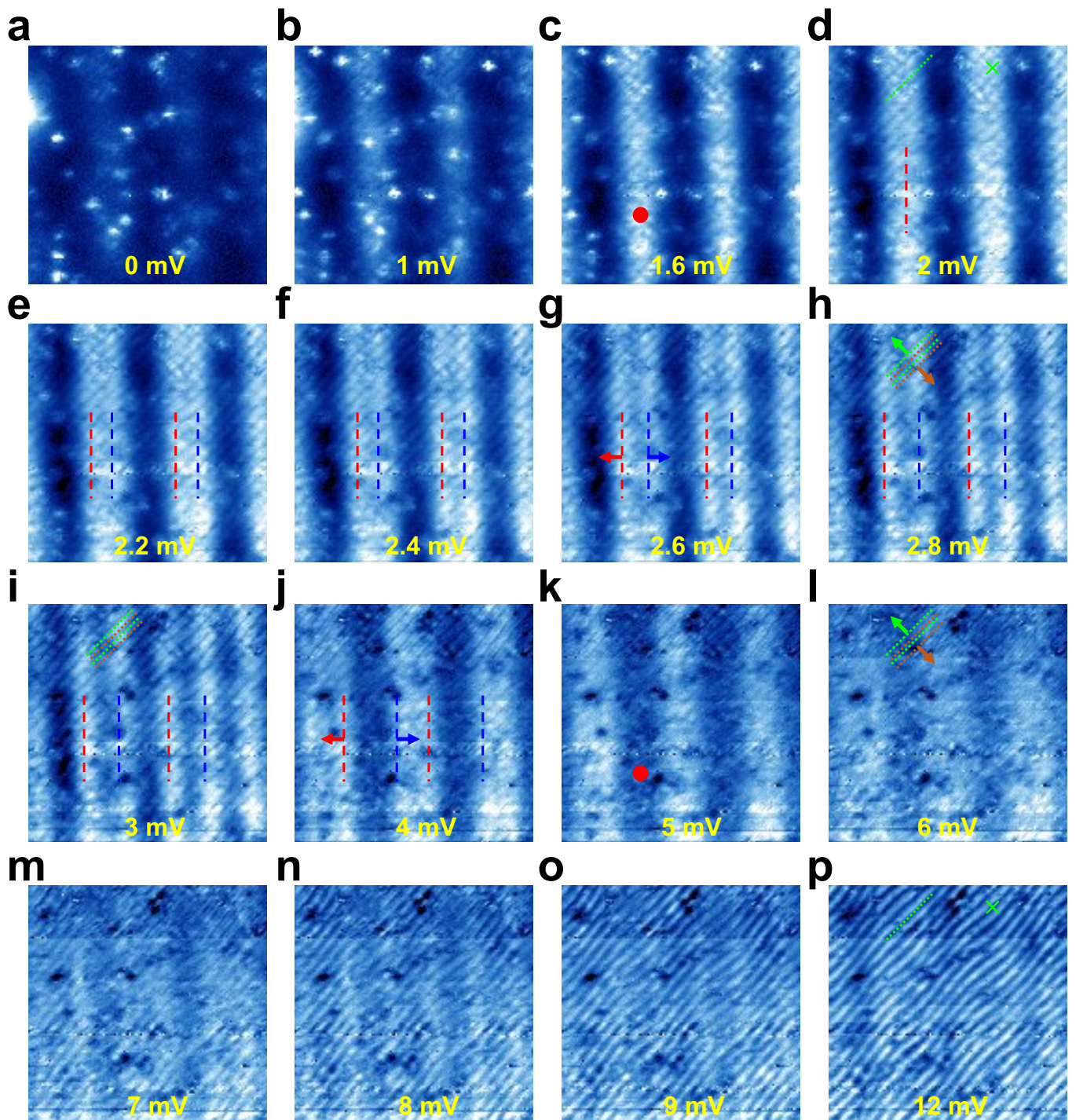**c** Biaxial CDW
2 nm

d 90.0°

e 84.4°

f 86.2°
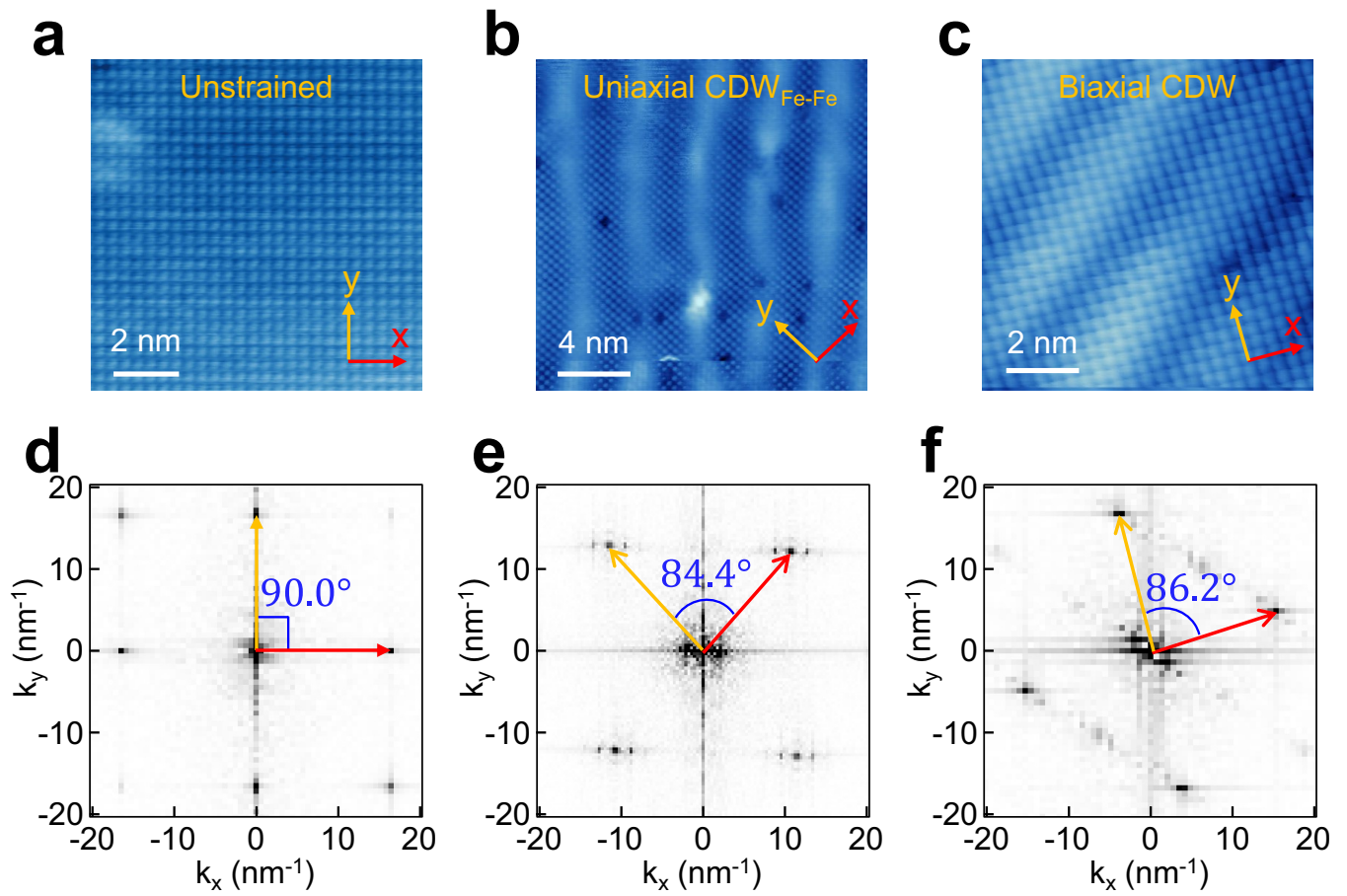
Extended Data Fig. 1 | Comparison of lattice distortion among different regions of LiFeAs. a–c, Atomic-resolution topographic images of the unstrained region, the uniaxial CDW$_{Fe-Fe}$ region and the biaxial CDW region. The crystallographic directions are shown in the lower right. **d–f**, Fourier transform images of **a–c**, respectively. The angles of the crystallographic directions are marked by coloured arrows.

Extended Data Fig. 2 | Evolution of the CDW_{As-As} and CDW_{Fe-Fe} stripes with bias voltages. a–p, dI/dV maps of a 70 nm × 70 nm biaxial CDW region under bias voltages of 0, 1.0, 1.6, 2.0, 2.2, 2.4, 2.6, 2.8, 3.0, 4.0, 5.0, 6.0, 7.0, 8.0, 9.0 and 12.0 mV, respectively. The red dot markers in **c** and **k** outline the π phase shift of the CDW_{As-As} pattern below and above the superconducting gap. The green cross markers in **d** and **p** outline the π phase shift of the CDW_{Fe-Fe} pattern below and above the superconducting gap. The CDW_{As-As} pattern shows a splitting behaviour of the stripes, which starts at an energy of approximately 2.2 mV (**e**). The stripes split into two sets, as highlighted by red and blue dashed lines (**e–j**). Each set of the stripes keeps the same periodicity with the original CDW_{As-As} stripes. However, both sets show dynamical behaviour with energy by moving in opposite directions, as highlighted by the red and blue arrows (**g**, **j**). At an energy of -4 mV, the split stripes recombine, returning back into a single set of stripes (**j**, **k**), with a π phase shift (**c**, **k**). Similar splitting–recombining behaviour exists in the CDW_{Fe-Fe} stripes. The splitting starts at an energy of approximately 2.8 mV, as highlighted by green and brown dotted lines (**h**). The recombination happens at approximately 9 mV, which is accompanied by a π phase shift (**d**, **p**). The same behaviour happens on the negative-bias side for the CDW_{As-As} and CDW_{Fe-Fe} stripes. The full set of dI/dV maps can be found in Supplementary Video 1. The evolution of the uniaxial CDW_{Fe-Fe} stripes can be found in Supplementary Video 2.
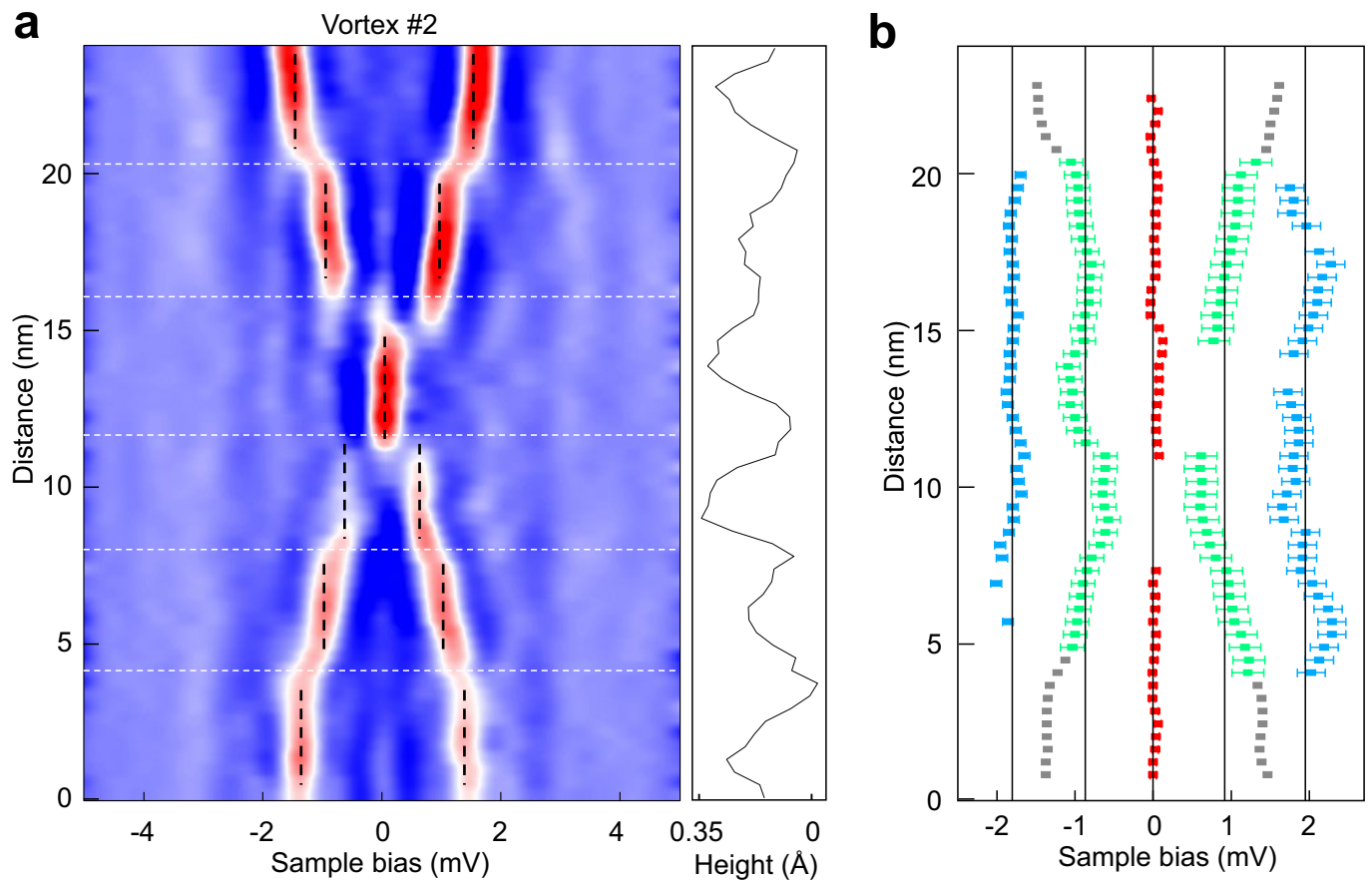
Extended Data Fig. 3 | Detailed analysis of the negative second derivative of the intensity plot of the dI/dV spectra across vortex #2. a, Left, Intensity map of $-\mathrm{d}^3I/\mathrm{d}V^3$ spectra across a topological vortex (vortex #2) along the As–As direction. The vertical black dashed lines outline the positions of the discrete vortex core states. The bound states show spatial dispersion of peak positions, similar to that observed in vortex #1. The horizontal white dashed lines outline the positions of dark stripes of CDW_{Fe-Fe}, in accordance with the height profile at right. The spatial variations of the vortex bound states happen in the vicinity of the positions of the dark stripes of CDW_{Fe-Fe}, suggesting a signature of the hybridization of the core states, which is a consequence of C_4 rotation and reflection-symmetry breaking. **b**, Statistical analysis of the peak positions in **a**. Five energy bound states at -1.81 ± 0.08 (L_{-2}), -0.87 ± 0.15 (L_{-1}), 0.03 ± 0.04 (L_0), 0.92 ± 0.20 (L_1) and 1.95 ± 0.19 (L_2) meV are extracted.
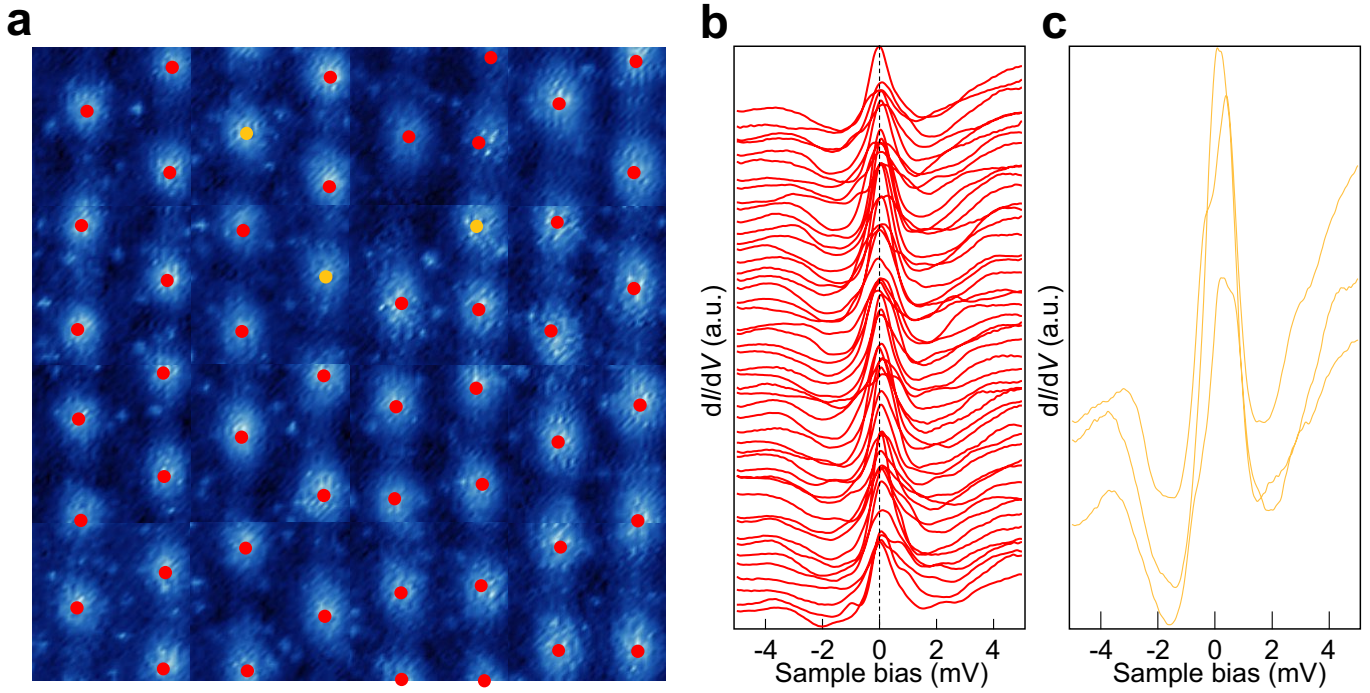
Extended Data Fig. 4 | Statistics of the topological and ordinary vortices in the MZM lattice. a, dI/dV map of the large-scale vortices at 0 mV. The red dots mark the vortices with sharp ZBCP (topological) of the MZMs, and the yellow dots mark the vortices without sharp ZBCP (ordinary). The spectra are calibrated by the multi-Gaussian peak fitting to extract the accurate energy positions of the vortex bound states. 48 out of 51 vortices show the sharp ZBCP at the centres. The scanning area is 200 nm × 200 nm. **b**, **c**, Individual dI/dV spectrum at each of the topological (**b**) and ordinary (**c**) vortices. More than 90% of the vortices have the characteristics of the MZM.
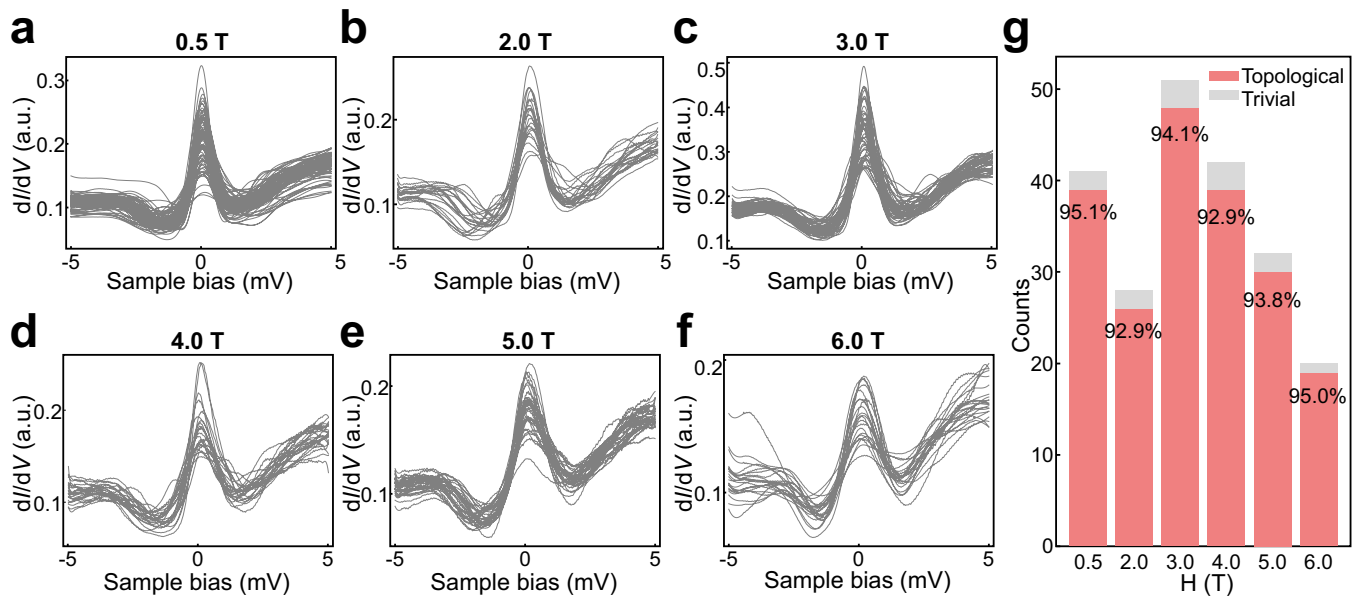
Extended Data Fig. 5 | Statistics of MZMs under different magnetic fields.
a–**f**, dI/dV spectra taken at the centres of different vortex cores under different magnetic fields. **g**, Histogram and percentage of topological vortices under different magnetic fields. The percentage of topological vortices is above 90% at all the magnetic fields up to 6 T.
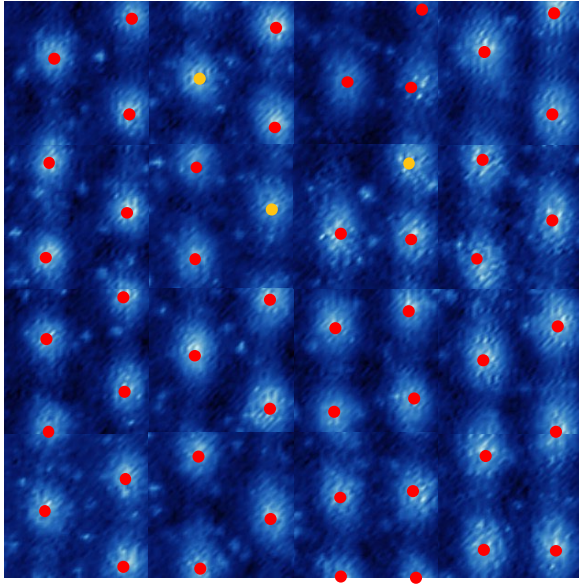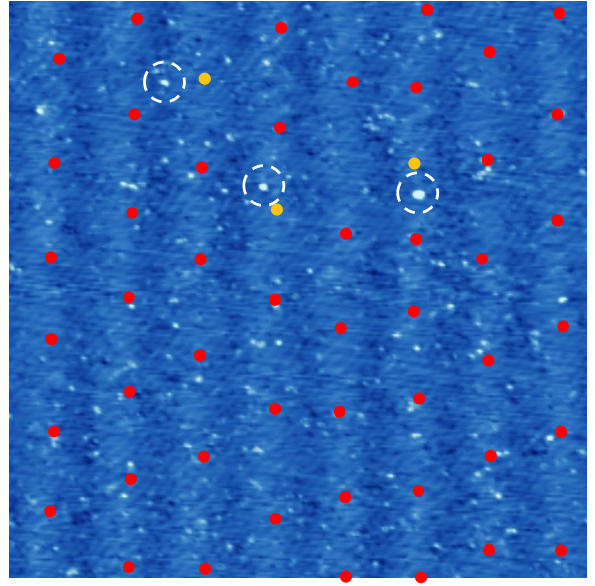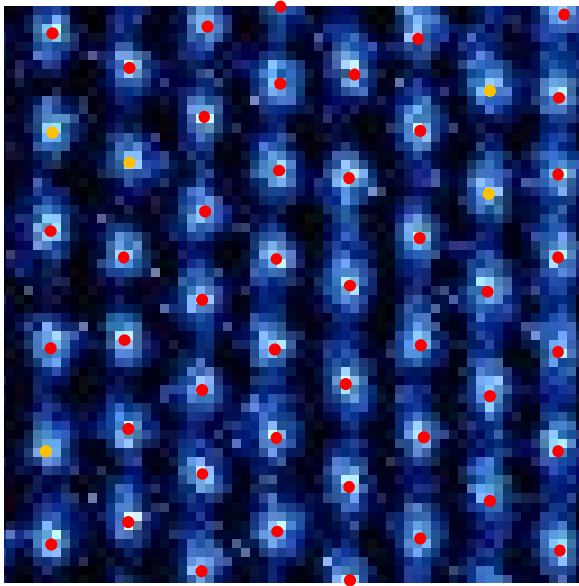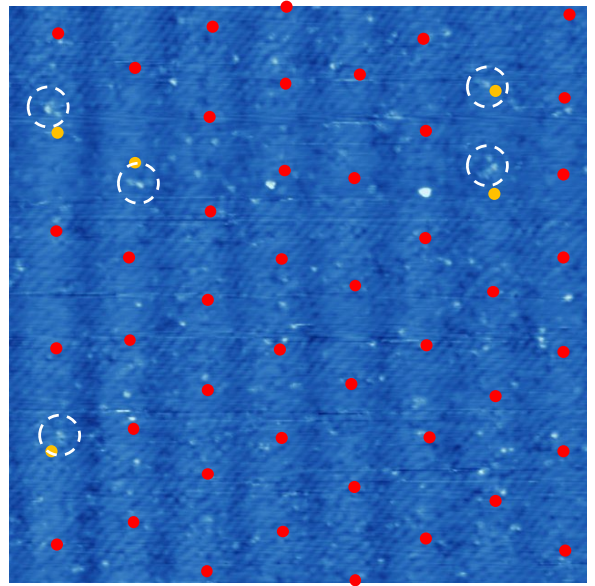
Extended Data Fig. 6 | Possible defect-induced topological–trivial vortex transition. a, Vortex lattice in the first round of measurement under a magnetic field of 3 T. The red and yellow dots represent topological and trivial vortices, respectively. **b**, Topographic image of the same region in **a**. The positions of the topological and trivial vortices are overlaid. **c**, Vortex lattice of the second round of measurement after the field is ramped down to 0 and then back to 3 T. The red and yellow dots represent topological and trivial vortices, respectively. **d**, Topographic image of the same region in **c**. The positions of the topological and trivial vortices are overlaid. The white dashed circles in **b** and **d** mark the positions of the impurities. Although the trivial vortices appear in different regions for the two rounds of measurements, they are all located in the vicinity of the impurities ('brighter dots'), as outlined by the white dashed circles in **b** and **d**.
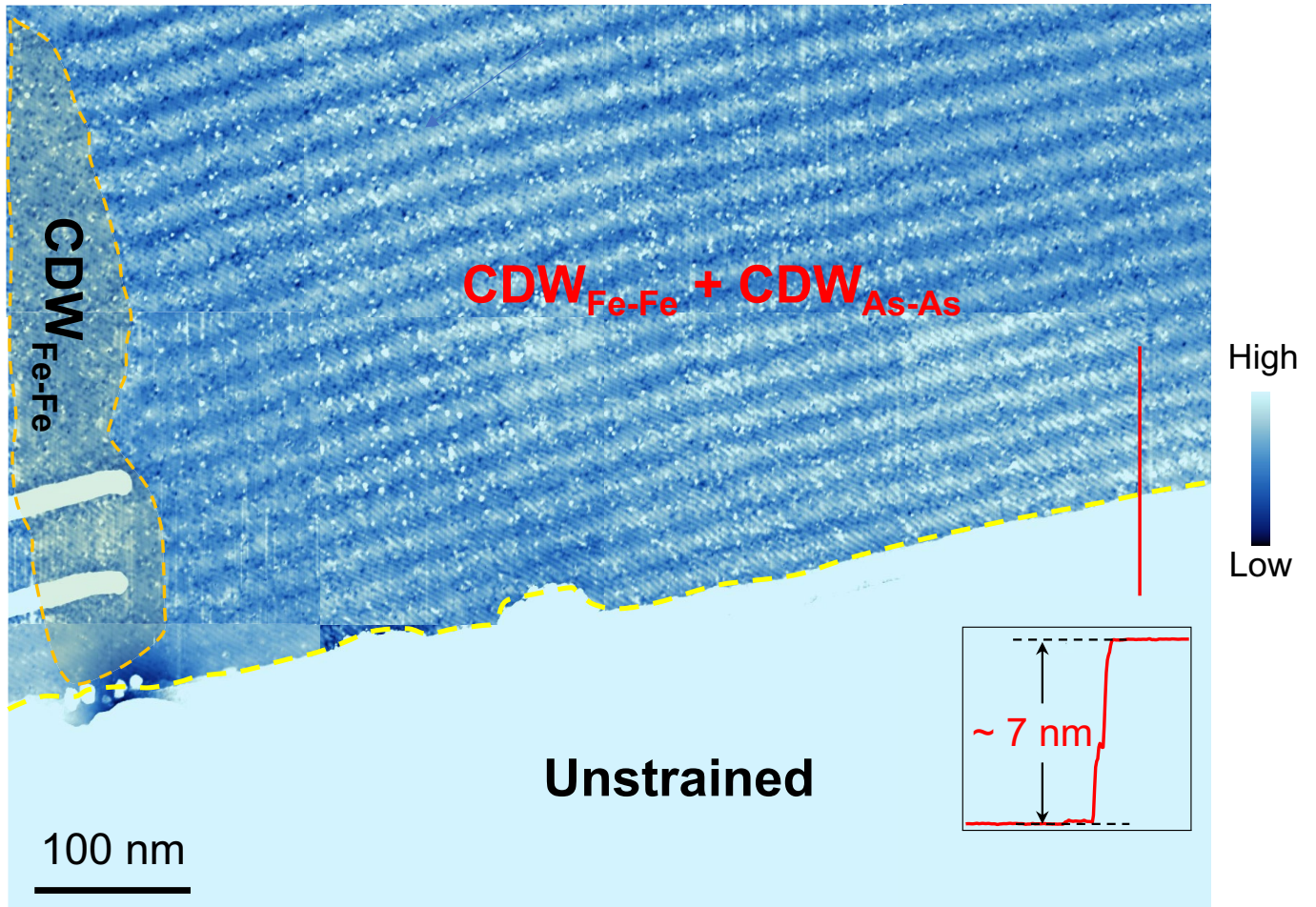
Extended Data Fig. 7 | Large-scale STM image of the strained and unstrained regions of the LiFeAs. The large-scale image is stitched together from 12 independent STM topographic images. The strained region locates between two big steps with heights of approximately 7 nm, consisting of two kinds of regions, the uniaxial CDW_{Fe-Fe} (upper left) and the biaxial CDW (upper right) regions, $V_s = -20$ mV, $I_t = 30$ pA.
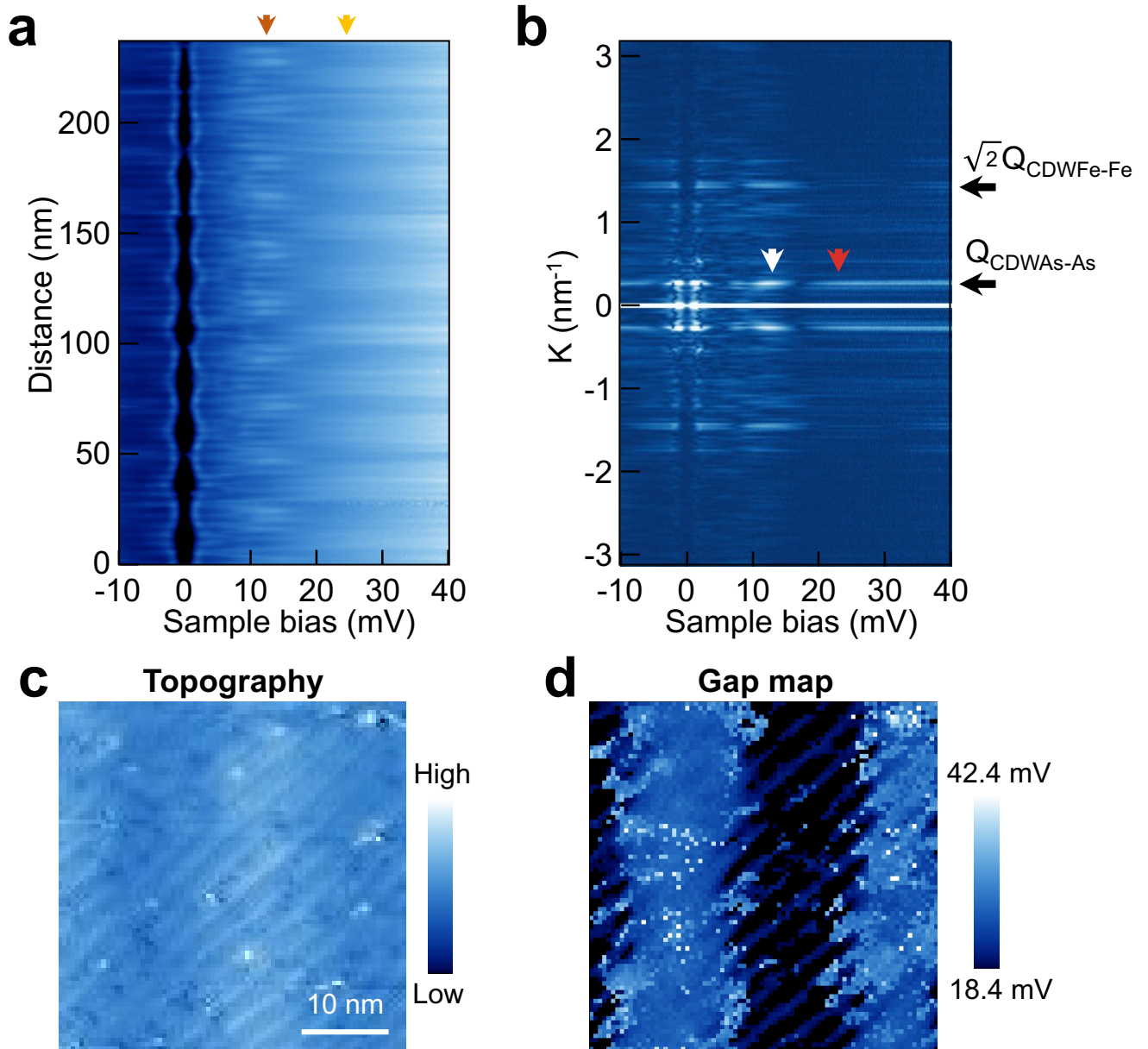
Extended Data Fig. 8 | Spatially dependent modulation of the CDW gap in the strained region. a, **b**, dI/dV spectra across the strained region (**a**) and the corresponding Fourier transform image (**b**). The hump features at energies of approximately 13 mV and roughly 22 mV are modulated by the As–As stripes. **c**, **d**, STM image (**c**) and CDW_{As-As} gap map (**d**) of the biaxial CDW region. The CDW gap is extracted by calculating the peak-to-peak values of the CDW coherence peaks, as labelled in Supplementary Fig. 7. The gap value is strongly modulated by the As–As stripes in a way that the gap sizes on the As–As stripes are lower than off the stripes (in **c**: $V_s = -15$ mV, $I_t = 200$ pA).
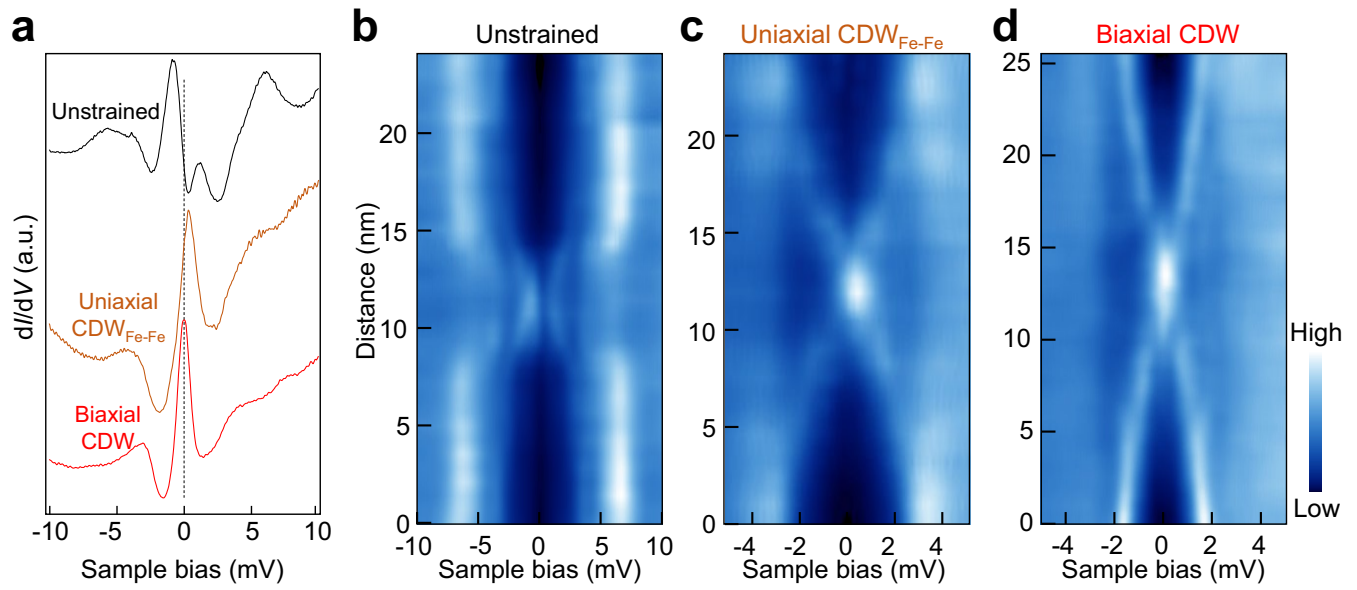
Extended Data Fig. 9 | Comparison of the spectral feature of the vortices in the unstrained, uniaxial CDW_Fe–Fe and biaxial CDW regions. a, dI/dV spectra taken at the centres of ordinary vortices in the unstrained (black), the uniaxial CDW_Fe–Fe region (brown) and a topological vortex in the biaxial CDW region (red). **b**, Intensity map of the dI/dV linecut across the ordinary vortex in the unstrained region. **c**, Intensity map of the dI/dV linecut across the ordinary vortex in the uniaxial CDW_Fe–Fe region. **d**, Intensity map of the dI/dV linecut across the topological vortex in the biaxial CDW region. The topological vortices exist only in the biaxial CDW regions.
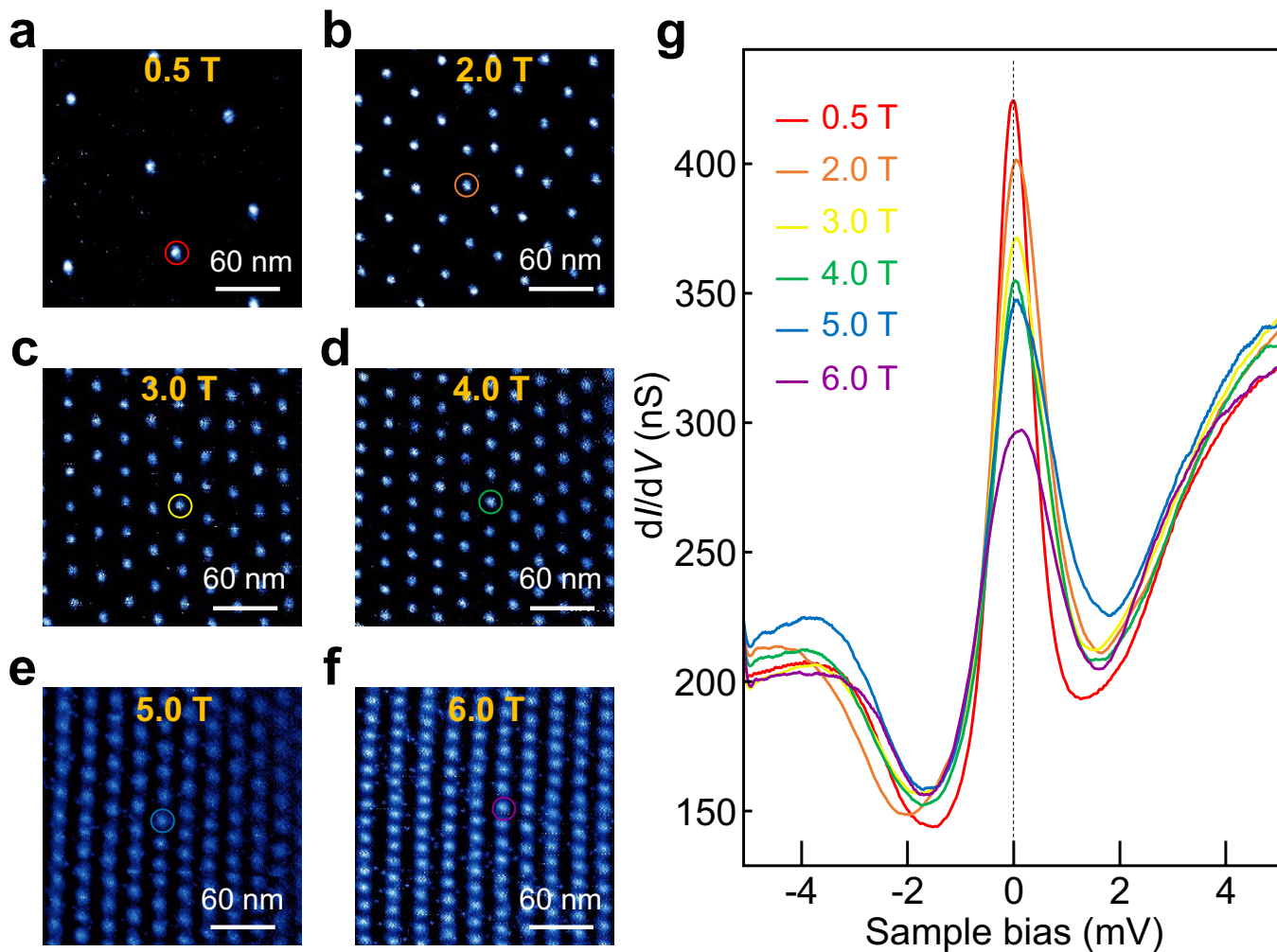
Extended Data Fig. 10 | Correlation between the vortex spacing and the dI/dV spectra of the MZM vortices. a–**f**, dI/dV maps of MZM lattices at 0 mV under magnetic fields from 0.5 T to 6 T, respectively. **g**, Averaged dI/dV spectra under different magnetic fields. The spectra are taken under the same scanning settings. With increasing magnetic fields, the ZBCPs of the dI/dV spectra get lower and broader. This phenomenon indicates that a coupling of the MZMs appears when the vortices get closer to each other under higher magnetic fields. The averaged dI/dV spectra under different fields can be found in Supplementary Video 3.